Pancake-like $Fe_2(MoO_4)_3$ microstructures: microwave-assisted hydrothermal synthesis, magnetic and photocatalytic properties†

Lei Zhang,[a] Xiao-Feng Cao,[a] Ying-Li Ma,[a] Xue-Tai Chen*[a] and Zi-Ling Xue[b]

Received (in Montpellier, France) 22nd January 2010, Accepted 3rd May 2010
DOI: 10.1039/c0nj00048e

A fast and economical route based on microwave-assisted hydrothermal reaction has been developed to synthesize pancake-like $Fe_2(MoO_4)_3$ microstructures. The phase and morphology of the products have been characterized by powder X-ray diffraction (XRD), energy dispersive spectrometry (EDS), selected area electron diffraction (SAED), high resolution transmission electron microscopy (HRTEM) and scanning electron microscopy (SEM). Several factors, including the amount of nitric acid, reaction time, temperature and iron source, play crucial roles in the formation of the $Fe_2(MoO_4)_3$ multilayer stacked structures. Detailed studies indicate that the oriented attachment and layer-by-layer self-assembly of nanosheets is responsible for the formation of these structures. The magnetic and photocatalytic properties of the product have also been investigated.

Introduction

Hydrothermal synthesis is a well-established approach for the preparation of various functional nanomaterials with desired micro/nanostructures. It has demonstrated advantages in the processing of nanostructural materials for a variety of potential applications in, *e.g.*, electronics, optoelectronics, catalysis, ceramics, magnetic data storage, biomedical and biophotonics.[1–6] Usually the nucleation and growth of nanocrystals are initiated during the hydrothermal process. In particular, the formation of crystalline products through hydrothermal process can be produced at temperatures substantially lower than those required by conventional solid-state or vapor reactions.[7–9] However, conventional heating in hydrothermal process is inevitably confronted with several disadvantages, such as sharp thermal gradients throughout the bulk solution, slow reaction kinetics and nonuniform reaction conditions.[10–12] In recent years, microwave heating has been widely applied in chemical reactions and materials synthesis, and it has demonstrated several advantages: (1) shorter reaction time; (2) more uniform product dimensions and composition; (3) easiness to tune compositions of the products.[13–19]

As a family of important functional materials, metal molybdates have been widely used in photoluminescence, microwave applications, optical fibers, scintillator materials, humidity sensors, and catalysis.[20–25] Iron molybdate is a particularly efficient catalyst for the oxidation of methanol to formaldehyde[26] and exhibits very interesting magnetic properties.[27] Traditionally iron molybdates were prepared *via* high temperature solid-state reactions.[28–30] Several solution-phase routes have already been employed to controllably prepare this functional nanomaterial. For example, Ding and co-workers[31] have designed a template-free hydrothermal process to selectively prepare monoclinic and orthorhombic $Fe_2(MoO_4)_3$ microsized particles with complex three-dimensional architectures. These reported procedures usually require a long reaction time. A facile and fast solution-based procedure is highly desired for the preparation of iron molybdates. Recently, our group has developed a microwave-assisted solution-phase route for the preparation of iron molybdates. Employing this technique, $FeMoO_4$ hierarchical hollow spheres with 1.0 μm in diameter have been prepared.[32] In this paper, we report the successful synthesis of pancake-like $Fe_2(MoO_4)_3$ microstructures *via* a facile and rapid microwave-assisted hydrothermal route. To the best of our knowledge, there has been no report on the preparation of such $Fe_2(MoO_4)_3$ microstructures. By controlling the experimental parameters, such as the amount of nitric acid, reaction time, temperature and iron source, novel $Fe_2(MoO_4)_3$ multilayer stacked structures have been successfully fabricated. Moreover, the magnetic and photocatalytic properties of the product were studied.

Experimental section

All reagents were purchased from Shanghai Chemical Company and used without further purification. All the samples were prepared in a microwave system (2.45 GHz, 200 W, Discover S-Class, CEM). The system was equipped with *in situ* magnetic stirring. The exposure time and temperature were programmed. The automatic temperature-control system allowed continuous monitoring and control (1 °C) of the internal temperature of reaction system. The preset profile (desired time and temperature) was followed automatically by continuously adjusting the

[a] *State Key Laboratory of Coordination Chemistry, Nanjing National Laboratory of Microstructures, School of Chemistry and Chemical Engineering, Nanjing University, Nanjing 210093, P. R. China. E-mail: xtchen@netra.nju.edu.cn; Fax: +86 25-83314502*
[b] *Department of Chemistry, The University of Tennessee, Knoxville, Tennessee 37996-1600, USA*

† Electronic supplementary information (ESI) available: SEM images and XRD patterns of the products at different reaction temperatures or different volumes of dilute nitric acid; SEM image and XRD pattern of the product obtained before microwave treatment; the TG curve of pancake-like $Fe_2(MoO_4)_3$ microstructures. See DOI: 10.1039/c0nj00048e

applied microwave power. The preparation of dilute nitric acid: 1 mL of concentrated nitric acid (wt 65%) was mixed with 19 mL of water. In a typical preparation procedure, $Fe(NO_3)_3{\cdot}9H_2O$ (0.404 g, 1.0 mmol) and $(NH_4)_6Mo_7O_4{\cdot}4H_2O$ (0.2648 g, 0.214 mmol) was dissolved in 7 mL of distilled water, respectively. $(NH_4)_6Mo_7O_4{\cdot}4H_2O$ solution was added dropwise to the $Fe(NO_3)_3{\cdot}9H_2O$ solution under magnetic stirring. Then additional 1 mL of the above-prepared dilute nitric acid was added. The mixture was transferred to a 35 mL round-bottom flask. After treating the mixture at 150 °C for 1 min under microwave irradiation, it was cooled to room temperature rapidly by air compressor. The product was collected, washed with deionized water and absolute ethanol, and dried in a vacuum at 60 °C for 6 h with a yield of 90%.

The products were characterized by X-ray powder diffraction (XRD) with a Shimadzu XRD-6000 powder X-ray diffractometer with CuKα radiation (λ = 1.5418 Å), recorded with 2θ ranging from 10° to 50°. HRTEM were carried out on a JEM-2100 high resolution transmission microscope, employing an accelerating voltage of 200 kV. SEM images and EDS of the products were obtained on field emission scanning electron microanalysers (Hitachi S-4800), employing the accelerating voltage of 5 or 20 kV. The magnetic property of the product was obtained on superconducting quantum interference device (SQUID) magnetometer (Quantum Design). Thermogravimetric analysis (TGA) was carried out on a Pyris 1 TGA thermal analyzer (PerkinElmer) with a heating rate of 10 °C min^{-1}.

The photocatalytic degradation of bromo-pyrogallol red was conducted in an XPA-photochemical reactor (Xujiang Electromechanical Plant, Nanjing, China) equipped with 500 W Xe lamp and a cutoff filter (λ > 420 nm). An electric fan and cycled condensate water were used to prevent thermal catalytic effects. $Fe_2(MoO_4)_3$ photocatalyst (0.02 g) was introduced into each of a series of Pyrex reactors containing 25 mL of bromo-pyrogallol red aqueous solution (0.01 g L^{-1}) at room temperature under air, respectively. Before light was turned on, the solution was continuously stirred for 30 min in the dark to ensure the establishment of an adsorption–desorption equilibrium. During irradiation, one Pyrex reactor was taken out at given time intervals. During the photocatalytic process, the color of the dye solution gradually faded with increasing exposure time. The photocatalyst powders and the dye solution were separated by a centrifugal machine. The bromo-pyrogallol red concentration was analyzed through a UV-vis spectrophotometer (Shimadzu, UV-3600).

Results and discussion

Fig. 1 depicts the XRD pattern of the product prepared at 150 °C for 1 min. All the reflection peaks could be indexed to monoclinic $Fe_2(MoO_4)_3$ with calculated lattice constants of a = 15.72 Å, b = 9.24 Å, and c = 18.22 Å, which is in good agreement with the literature values (JCPDS file Card No. 35–0183). No other impurity peak is detected. Additional evidence of the formation of $Fe_2(MoO_4)_3$ comes from energy dispersion X-ray analysis. Fig. 2 shows the energy dispersion X-ray spectrum (EDS) of the as-prepared product.

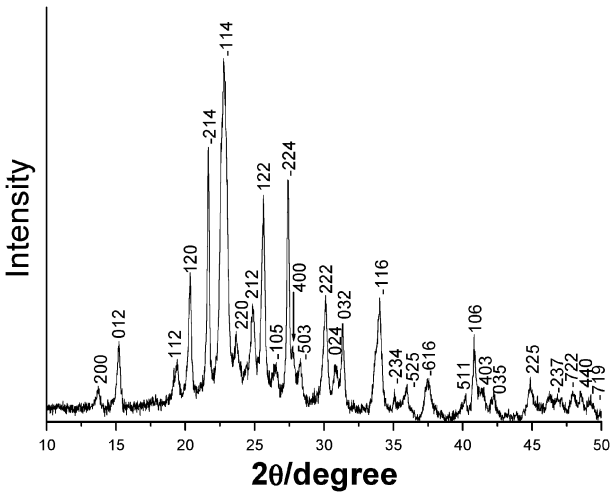

Fig. 1 The XRD patterns of the product prepared at 150 °C for 1 min under microwave irradiation.

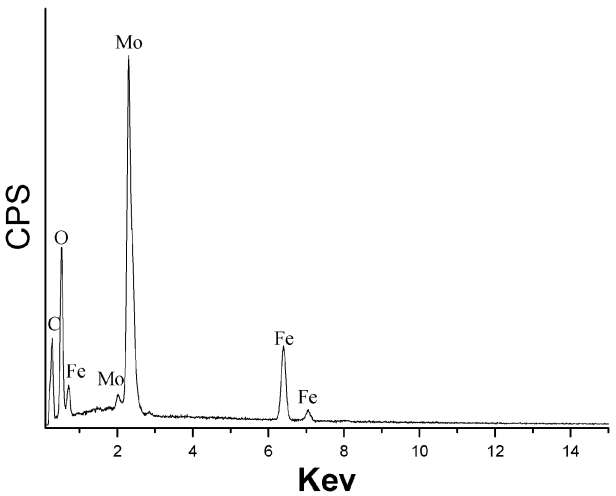

Fig. 2 The EDS spectrum of the product prepared at 150 °C for 1 min under microwave irradiation.

The peaks of Fe, Mo and O can be easily found. The C peak in the spectrum can be attributed to CO_2 adsorbed by the sample.

The microstructure and morphology of the product were also investigated by SEM and HRTEM. As shown in Fig. 3a and b, the as-prepared product is composed of pancake-like $Fe_2(MoO_4)_3$ microstructures with relatively good dispersion and uniform diameters of ~5 μm. A high magnification SEM image shown in Fig. 3c reveals that the building blocks of such nanoarchitectures are nanosheets with ~40 nm in mean thickness. Fig. 3d shows a typical TEM image of the product, which further confirms the result of SEM. Fig. 3e shows a broken flake of these aggregations prepared by microwave irradiation for one minute. The selected area electron diffraction (SAED) pattern and high resolution TEM were used to examine its crystal structure. The SAED pattern recorded on this broken flake of the product proves the single-crystalline nature of the building blocks (Fig. 3f).

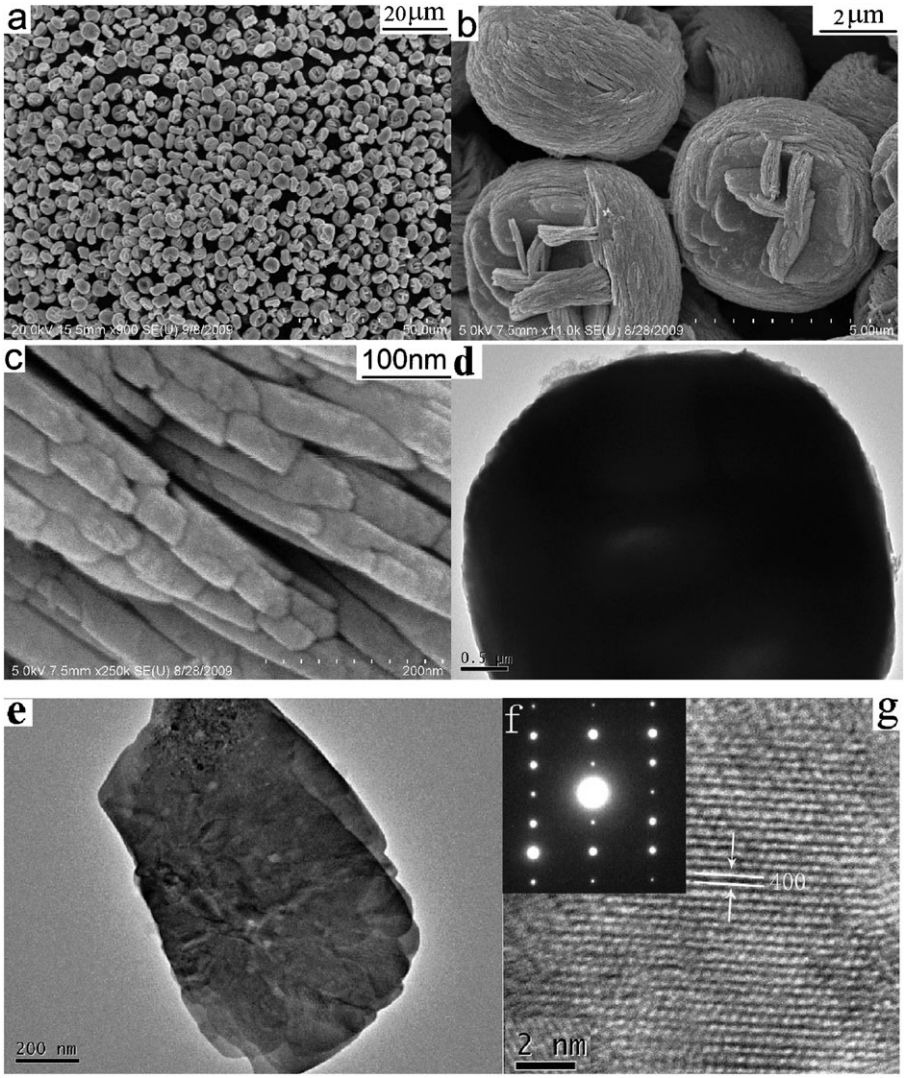

Fig. 3 SEM images (a–c), TEM images (d and e), SAED pattern (f) and HRTEM image (g) of the as-prepared $Fe_2(MoO_4)_3$ at 150 °C for 1 min under microwave irradiation.

The clear interlaced stripes further confirm its single crystalline nature. According to the measurements, the distances between the neighboring planes are 0.3211 nm, corresponding to (400) plane of $Fe_2(MoO_4)_3$ (Fig. 3g).

To investigate the effect of other reaction parameters such as the reaction temperature, the amount of nitric acid, and iron sources, comparison experiments were designed. It has been found that the morphology of the final product is strongly dependent on the reaction temperature. When the reaction was carried out at 120 °C, keeping the total volume constant, many irregular nanoparticles were obtained (ESI†, Fig. S1a). The corresponding XRD shown in Fig. S2a indicates that the phase of the product is amorphous, which implies that 120 °C is not high enough for the crystallization of $Fe_2(MoO_4)_3$. Increasing the temperature to 180 °C, pancake-like $Fe_2(MoO_4)_3$ microstructures appeared (ESI†, Fig. S1b and S2b). A local enlargement SEM image of the region, indicated by an arrow in Fig. S1b, reveals that nanowires are simultaneously obtained (ESI†, Fig. S1c). These experiments indicate that the reaction temperature is undoubtedly indispensable for the formation of pancake-like $Fe_2(MoO_4)_3$ microstructures and 150 °C is found to be optimum.

The amount of nitric acid is an important factor affecting the formation of pancake-like $Fe_2(MoO_4)_3$ microstructures. The SEM images and XRD patterns of the products obtained at different amount of nitric acid are shown in Fig. S3 and S4 (ESI†). When the experiment was carried out in the absence of dilute nitric acid, the product was comprised of random aligned multilayer stacked structures of $Fe_2(MoO_4)_3$ with diameters of ~8 μm (ESI†, Fig. S3a–b and S4a). When 0.5 mL of the above-prepared dilute nitric acid was added (pH = 1.03), keeping other experimental parameters constant, well-aligned multilayer stacked structures and nanoparticles were simultaneously produced (ESI†, Fig. S3c–d and S4b). Increasing the volume of the dilute nitric acid to 1 mL (pH = 0.88), monodisperse pancake-like $Fe_2(MoO_4)_3$ microstructures appeared (Fig. 3). Further increasing to 1.5 and 2 mL (pH = 0.75 and 0.61), the final products were also

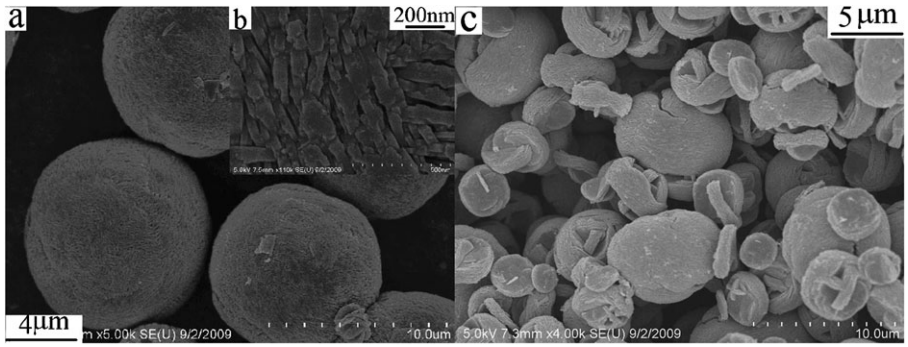

Fig. 4 SEM images of the products with different iron sources: (a and b) $FeCl_3{\cdot}6H_2O$ and (c) $Fe_2(SO_4)_3{\cdot}7H_2O$.

comprised of pancake-like $Fe_2(MoO_4)_3$ and nanoparticles (ESI†, Fig. S3e–h and S4c–d).

Different iron sources were tested to check their effects on the syntheses. When $Fe(NO_3)_3{\cdot}9H_2O$ was replaced by $FeCl_3{\cdot}6H_2O$, the final product was comprised of nanosheet-assembled $Fe_2(MoO_4)_3$ microspheres with diameters of $\sim$10 μm (Fig. 4a and b). If $Fe_2(SO_4)_3{\cdot}7H_2O$ was used, polydisperse $Fe_2(MoO_4)_3$ multilayer stacked structures were produced (Fig. 4c). Careful examinations indicate that the variation of iron sources did not change the morphology of these building blocks. However, it should be noted that there were major changes in the sizes, dispersion and morphology of these aggregations. These facts imply that the $Fe(NO_3)_3{\cdot}9H_2O$ is the appropriate iron source for the preparation of monodisperse pancake-like $Fe_2(MoO_4)_3$.

These morphological changes observed above may be ascribed to the difference of the nucleation and growth process under different reaction conditions. Usually, the initial tiny crystallites formed during the nucleation process serve as the core of the following crystal growth. Changes in the reaction conditions may lead to the different behavior in nucleation and crystal growth. Such morphological tuning has been well demonstrated by changing the experimental parameters such as reaction temperature, reaction time and pH value.[31,33,34]

In the CEM system we used, the automatic temperature-control and cooling system allowed for continuous monitoring and control (1 °C) of the internal temperature and rapidly cooling to room temperature within one minute. In order to monitor the morphological evolution and reveal the possible growth mechanism of the pancake-like $Fe_2(MoO_4)_3$ micro-structures, a series of time-dependent experiments were carefully carried out to gain an insight into the formation process. Before microwave treatment, the reaction mixture was centrifuged and the solid product was collected. Experiments indicated that the product was composed of amorphous nanoparticles with 100–200 nm in diameters (ESI†, Fig. S5). When the reaction time was controlled at 5 s, $Fe_2(MoO_4)_3$ nanoparticles were obtained (Fig. 5a and 6a). Prolonging the reaction time to 10 s, these

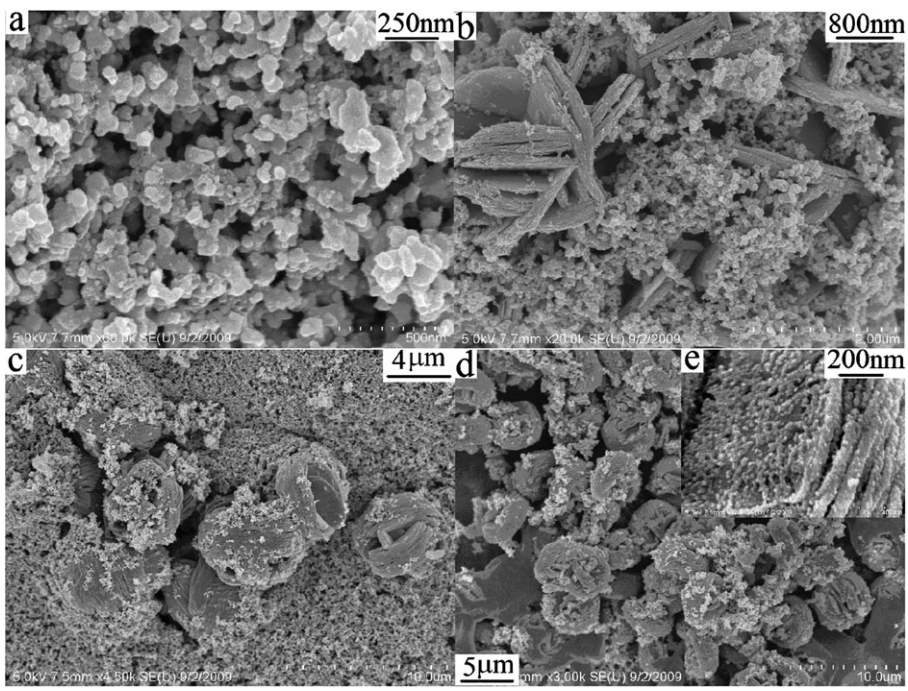

Fig. 5 SEM images of the products at 150 °C with different reaction times: (a) 5 s, (b) 10 s, (c) 15 s and (d and e) 40 s.

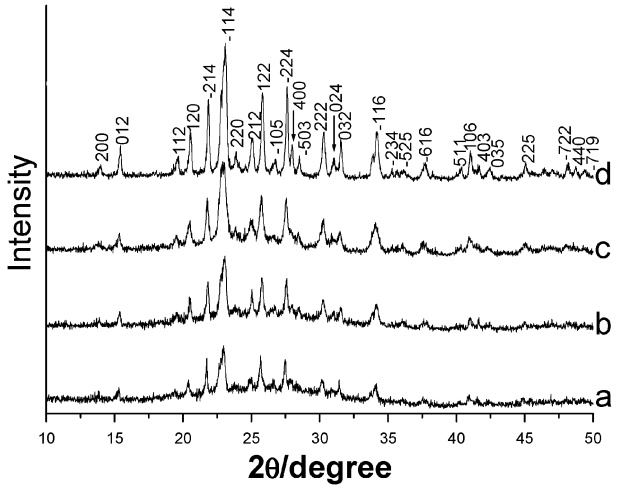

Fig. 6 The XRD patterns of the products with different reaction times: (a) 5 s, (b) 10 s, (c) 15 s and (d) 40 s.

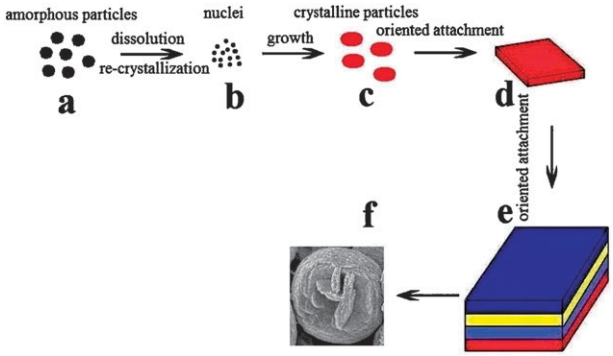

Scheme 1 The possible formation process of pancake-like $Fe_2(MoO_4)_3$ microstructures.

nanoparticles grew into nanosheets with large sizes (Fig. 5b and 6b). Pancake-like aggregations and nanoparticles coexisted in the final product after the mixture was aged for 15 s (Fig. 5c and 6c). After reaction for 40 s, more and more assembled plate-like $Fe_2(MoO_4)_3$ architectures came into being with nanoparticles attached to their surface (Fig. 5d, e and 6d). Finally, fully self-assembled pancake-like $Fe_2(MoO_4)_3$ microstructures were obtained after reaction for 1 min (Fig. 2).

As well known, there are generally two pathways with regard to the crystallization process. The first one is so-called classical crystallization in which the crystal grows on the stable nuclei *via* ion-by-ion addition and unit replication. The second one is nonclassical crystallization including oriented attachment and mesocrystallization.[35–40] Oriented attachment is described as the spontaneous assembly of adjacent particles sharing a common crystallographic orientation by crystallographic fusion at the planar interface. If the nanoparticles are coated by some organic components, they can form a mesocrystal *via* mesoscale assembly, possibly followed by fusion to an isooriented crystal and finally to a single crystal.[41–44] Based on the above experimental results, we consider that oriented attachment could be a dominant process in the layer-by-layer self-assembly of nanosheets and lead to the formation of such pancake-like $Fe_2(MoO_4)_3$ microstructures. Actually, this self-assembly model has already been demonstrated[45–48] and proven to be feasible to fabricate various functional multi-layers stacked structures. For example, Song *et al.*[48] reported the successful fabrication of layer-controlled hierarchical flower-like $AgIn(MoO_4)_2$ microstructures using submicroplates as building blocks *via* a layer-by-layer self-assembly process. Based on the literature, a schematic illustration of the formation mechanism for the fabrication of pancake-like $Fe_2(MoO_4)_3$ is proposed (Scheme 1). Before microwave treatment, amorphous nanoparticles were firstly produced (a, Scheme 1). Under the microwave-assisted hydrothermal conditions, the amorphous precipitates gradually dissolved and $Fe_2(MoO_4)_3$ nuclei formed (b, Scheme 1) and grew into crystalline nanoparticles with the proceeding of reaction (c, Scheme 1). The dissolution and sequential re-crystallization carried out a transformation from amorphous nanoparticles to crystalline ones. Such a growth process should be consistent with a solid–solution–solid transformation mechanism.[49] Then, adjacent particles with common crystallographic orientations could perform crystallographic fusion at the planar interface and further grew to nanosheets (d, Scheme 1). With the prolonging of reaction time, the layer-by-layer self-assembly of these building blocks would occur along a certain direction and lead to nanosheets-assembled microstructures (e, Scheme 1). Finally, the layer number of the superstructures gradually increased and fully self-assembled pancake-like $Fe_2(MoO_4)_3$ microstructures were produced (f, Scheme 1).

The thermal stability of pancake-like $Fe_2(MoO_4)_3$ microstructures is characterized by thermogravimetric analysis (TGA). The TGA plot reveals a small 1.4% weight loss for the sample in the temperature range from 100 °C to 700 °C (Fig. S6, ESI†), which is probably the loss of the surface water on the particles.[31] This result indicates that the product is quite stable at high temperature.

The magnetic properties of the as-obtained monoclinic $Fe_2(MoO_4)_3$ microstructures were investigated by using a superconducting quantum interference device (SQUID). Magnetization was measured in the temperature range between 1.8 and 300 K by using a SQUID (Quantum Design) magnetometer with 2000 Oe field strength. Fig. 7a and b shows temperature dependence of the inverse magnetic susceptibility and magnetic susceptibility obtained from monoclinic $Fe_2(MoO_4)_3$. As is shown in Fig. 7a, one can find that the reciprocal magnetic susceptibility and the temperature exhibit a linear relationship, which can be fitted to the Curie–Weiss law (eqn (1)).[27]

$$\chi = C/T - \Theta \qquad (1)$$

The curve fit between 50 and 300 K gives negative Curie–Weiss temperature $\Theta = -47$ K. $Fe_2(MoO_4)_3$ orders magnetically at 12 K as estimated from the temperature dependence of magnetic susceptibility at the constant field strength of 2000 Oe (Fig. 7b). The increase of magnetic susceptibility during cooling at about 12 K indicates a ferromagnetic component in the magnetic structure. Fig. 8a and b show the hysteresis loop of the as-synthesized product with the field sweeping from −70 to +70 kOe at $T = 1.8$ K. Below 12 K, hydrothermally obtained monoclinic $Fe_2(MoO_4)_3$

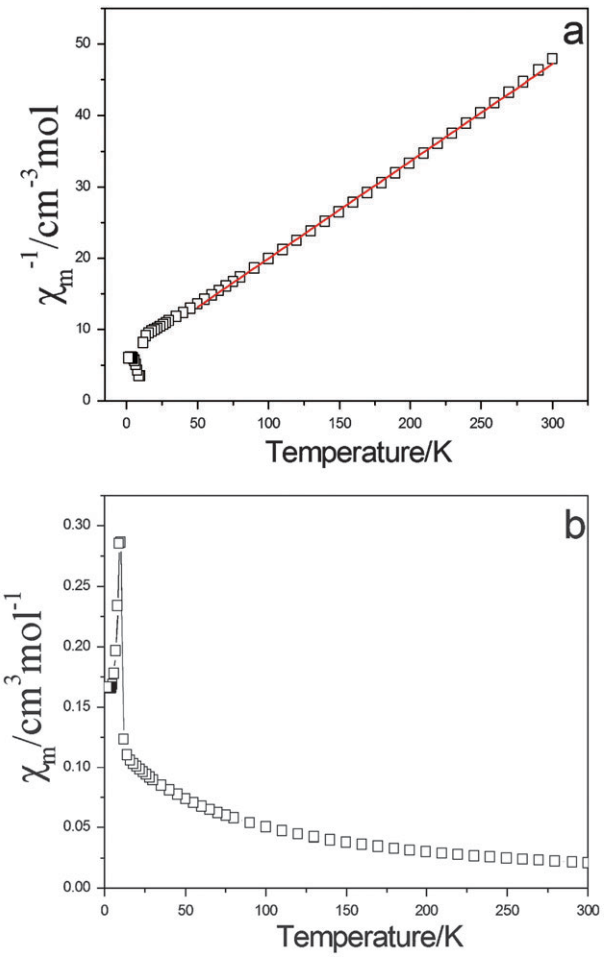

Fig. 7 Temperature dependence of (a) inverse magnetic susceptibility and (b) magnetic susceptibility.

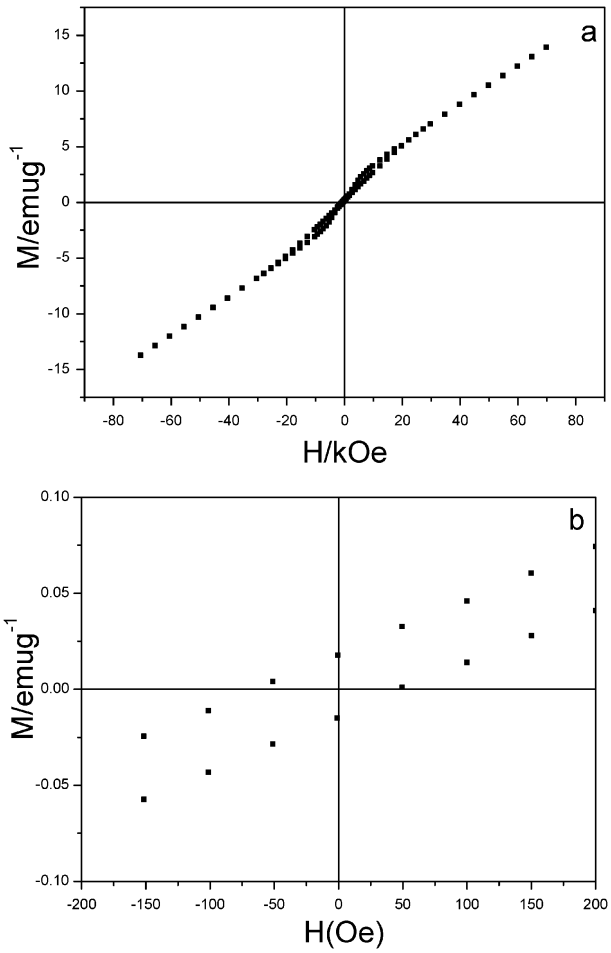

Fig. 8 M–H hysteresis loops of pancake-like $Fe_2(MoO_4)_3$ microstructures at 1.8 K (a) and partially enlarged M–H curve of Fig. 7c (b).

particles show ferromagnetic performance. Thus, the magnetic properties of the $Fe_2(MoO_4)_3$ product are similar to the reported results for $Fe_2(MoO_4)_3$.[27,31]

Recently, Yu *et al.* developed a facile hydrothermal route for the selective preparation of molybdate hydrates $MMoO_4 \cdot nH_2O$ (M = Co, Ni, Mn, n = 0, 3/4, 1) nano/microcrystals with different phases and morphologies.[50] $CoMoO_4$ nanorod bundles were found to exhibit a high photocatalytic activity for the degradation of acid fuchsine. To demonstrate the potential application of as-synthesized pancake-like $Fe_2(MoO_4)_3$ in the degradation of organic contaminants, we investigated the photocatalytic activities by choosing the photocatalytic degradation of bromo-pyrogallol red as a model reaction. As a comparison, direct photolysis of bromo-pyrogallol red was also performed under identical conditions. We observed that direct photolysis of bromo-pyrogallol red was negligible (only 3%) after 40 min of visible light irradiation (Fig. 9). In the presence of pancake-like $Fe_2(MoO_4)_3$, about 68% of bromo-pyrogallol was photolyzed under the same experimental conditions. When the other two catalysts obtained from different iron sources were used, they also exhibited similar photocatalytic activities. These results indicated that the $Fe_2(MoO_4)_3$ microstructures may find applications in water pollution control.

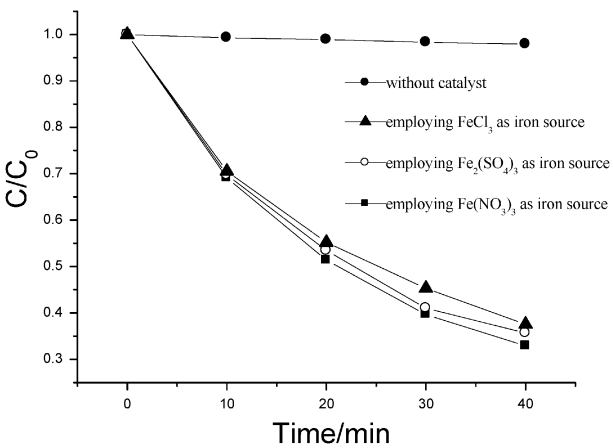

Fig. 9 Photodegradation efficiencies of bromo-pyrogallol red as a function of irradiation time with different catalysts.

Conclusions

Pancake-like $Fe_2(MoO_4)_3$ microstructures with relatively good dispersion and uniform diameters of $\sim$5 μm were successfully prepared *via* a facile and rapid microwave-assisted hydrothermal route. Experiments indicated that the amount of nitric acid,

reaction temperature, time and iron source could affect the formation and morphology of the product. The layer-by-layer self-assembly of nanosheets is responsible for the formation of such multilayer stacked structures. Experiments indicated that this pancake-like $Fe_2(MoO_4)_3$ displays ferromagnetic behavior at lower temperature. Furthermore, it also exhibits excellent photocatalytic property for the degradation of bromo-pyrogallol red. Compared to existing solution-phase synthetic methods using hydrothermal reaction, this combination of the microwave radiation and layer-by-layer self-assembly provides a facile, rapid, low-cost pathway to novel $Fe_2(MoO_4)_3$ nanoarchitectures.

Acknowledgements

This work was supported by the National Basic Research Program of China (No. 2006CB806104 and 2007CB925102), Natural Science Grant of China (No. 20721002), and the US National Science Foundation (CHE-051692).

References

1 K. Byrappa and T. Adschiri, *Prog. Cryst. Growth Charact. Mater.*, 2007, **53**, 117.
2 M. Rajamathi and R. Seshadri, *Curr. Opin. Solid State Mater. Sci.*, 2002, **6**, 337.
3 T. Xie, S. Li, W. B. Wang, Q. Peng and Y. D. Li, *Chem.–Eur. J.*, 2008, **14**, 9730.
4 Y. H. Ni, K. M. Liao, J. M. Hong and X. W. Wei, *CrystEngComm*, 2009, **11**, 570.
5 L. S. Zhang, W. Z. Wang, L. Zhou and H. L. Xu, *Small*, 2007, **3**, 1618.
6 H. P. Cong and S. H. Yu, *Cryst. Growth Des.*, 2009, **9**, 210.
7 L. Zhen, W. S. Wang, C. Y. Xu, W. Z. Shao and L. C. Qin, *Mater. Lett.*, 2008, **62**, 1740.
8 X. L. Hu, J. C. Yu and J. M. Gong, *J. Phys. Chem. C*, 2007, **111**, 11180.
9 X. Wang, J. Zhuang, Q. Peng and Y. D. Li, *Nature*, 2005, **437**, 121.
10 X. L. Hu, J. C. Yu, J. M. Gong and Q. Li, *Cryst. Growth Des.*, 2007, **7**, 2444.
11 S. H. Feng and R. R. Xu, *Acc. Chem. Res.*, 2001, **34**, 239.
12 M. Siskin and A. R. Katritzky, *Science*, 1991, **254**, 231.
13 G. A. Tompsett, W. C. Conner and K. S. Yngvesson, *ChemPhysChem*, 2006, **7**, 296.
14 I. Bilecka, I. Djerdj and M. Niederberger, *Chem. Commun.*, 2008, 886.
15 B. L. Newalkar, S. Komarneni and H. Katsuki, *Mater. Res. Bull.*, 2001, **36**, 2347.
16 B. Hu, S. B. Wang, K. Wang, M. Zhang and S. H. Yu, *J. Phys. Chem. C*, 2008, **112**, 11169.
17 J. C. Yu, X. L. Hu, Q. Li and L. Z. Zhang, *Chem. Commun.*, 2005, 2704.
18 S. H. Kim, S. Y. Lee, G. R. Yi, D. J. Pine and S. M. Yang, *J. Am. Chem. Soc.*, 2006, **128**, 10897.
19 J. C. Yu, X. L. Hu, Q. Li, Z. Zheng and Y. M. Xu, *Chem.–Eur. J.*, 2006, **12**, 548.
20 S. D. M. Jacques, O. Leynaud, D. Strusevich, A. M. Beale, G. Sankar, C. M. Martin and P. Barnes, *Angew. Chem., Int. Ed.*, 2006, **45**, 445.
21 W. X. Kuang, Y. N. Fan and Y. Chen, *Langmuir*, 2000, **16**, 5205.
22 A. W. Sleight and B. L. Chamberland, *Inorg. Chem.*, 1968, **7**, 1672.
23 Ü. Kersen and L. Holappa, *Appl. Phys. A: Mater. Sci. Process.*, 2006, **85**, 431.
24 A. W. Sleight, B. L. Chamberland and J. F. Weiher, *Inorg. Chem.*, 1968, **7**, 1093.
25 X. Y. Wu, G. R. Yu, X. C. Chen, Y. H. Wang and C. J. Liu, *Thermochim. Acta*, 2009, **486**, 20.
26 T. H. Kim, B. Ramachandra, J. S. Choi, M. B. Saidutta, K. Y. Choo, S. D. Song and Y. W. Rhee, *Catal. Lett.*, 2004, **98**, 161.
27 H. Ehrenberg, K. G. Bramnik, E. Muessig, T. Buhrmester, H. Weitzel and C. Ritter, *J. Magn. Magn. Mater.*, 2003, **261**, 353.
28 L. Wang, B. Peng, X. F. Guo, W. P. Ding and Y. Chen, *Chem. Commun.*, 2009, 1565.
29 I. Mitov, S. Asenov, T. Tomov and D. Klissurski, *J. Phys. Chem. C*, 2007, **111**, 5389.
30 A. P. V. Soares, M. F. Portela and A. Kiennemann, *Catal. Commun.*, 2001, **2**, 159.
31 Y. Ding, S. H. Yu, C. Liu and Z. A. Zang, *Chem.–Eur. J.*, 2007, **13**, 746.
32 L. Zhang, X. F. Cao, Y. L. Ma, X. T. Chen and Z. L. Xue, *CrystEngComm*, 2010, **12**, 207.
33 Y. W. Jun, S. M. Lee, N. J. Kang and J. Cheon, *J. Am. Chem. Soc.*, 2001, **123**, 5150.
34 Y. H. Kim, Y. W. Jun, B. H. Jun, S. M. Lee and J. Cheon, *J. Am. Chem. Soc.*, 2002, **124**, 13656.
35 Z. Liu, X. D. Wen, X. L. Wu, Y. J. Gao, H. T. Chen, J. Zhu and P. K. Chu, *J. Am. Chem. Soc.*, 2009, **131**, 9405.
36 Q. Zhang, S. J. Liu and S. H. Yu, *J. Mater. Chem.*, 2009, **19**, 191.
37 G. B. Cai, S. F. Chen, L. Liu, J. Jiang, H. B. Yao, A. W. Xu and S. H. Yu, *CrystEngComm*, 2010, **12**, 234.
38 S. J. Liu, J. Y. Gong, B. Hu and S. H. Yu, *Cryst. Growth Des.*, 2009, **9**, 203.
39 R. L. Penn and J. F. Banfield, *Science*, 1998, **281**, 969.
40 V. M. Yuwono, N. D. Burrows, J. A. Soltis and R. L. Penn, *J. Am. Chem. Soc.*, 2010, **132**, 2163.
41 H. Cölfen and M. Antonietti, *Angew. Chem., Int. Ed.*, 2005, **44**, 5576.
42 S. Wohlrab, N. Pinna, M. Antonietti and H. Cölfen, *Chem.–Eur. J.*, 2005, **11**, 2903.
43 A. W. Xu, M. Antonietti, H. Cölfen and Y. P. Fang, *Adv. Funct. Mater.*, 2006, **16**, 903.
44 M. Niederberger and H. Cölfen, *Phys. Chem. Chem. Phys.*, 2006, **8**, 3271.
45 C. X. Xu, X. Wei, Y. M. Guo, H. Q. Wu, Z. H. Ren, G. Xu, G. Shen and G. R. Han, *Mater. Res. Bull.*, 2009, **44**, 1635.
46 J. F. Shen, Y. Z. Hu, C. Li, C. Qin, M. Shi and M. X. Ye, *Langmuir*, 2009, **25**, 6122.
47 Y. X. Zhou, H. B. Yao, Q. Zhang, J. Y. Gong, S. J. Liu and S. H. Yu, *Inorg. Chem.*, 2009, **48**, 1082.
48 S. Y. Song, Y. Zhang, J. Feng, Y. Xing, Y. Q. Lei, W. Q. Fan and H. J. Zhang, *Cryst. Growth Des.*, 2009, **9**, 848.
49 Z. Y. Wu, X.J. Wang and Q. S. Huang, *Phys. Status Solidi B*, 1999, **213**, 343.
50 Y. Ding, Y. Wan, Y. L. Min, W. Zhang and S. H. Yu, *Inorg. Chem.*, 2008, **47**, 7813.